ChemCatChem

Research Article
doi.org/10.1002/cctc.202301673

Chemistry Europe
European Chemical Societies Publishing

www.chemcatchem.org

Impact of Ceria Support Morphology on Au Single-Atom Catalysts for Benzyl Alcohol Selective Oxidation

Xinyue Zhou,[a, b] Aristarchos Mavridis,[a] Mark A. Isaacs,[c, d] Charalampos Drivas,[a, b] Carmine D'Agostino,[a, e] and Christopher M. A. Parlett*[a, b, f]

Alcohol oxidations are a key industrial chemical transformation, with aldehydes and ketones finding use in an array of applications. Nobel metals are known for their activity towards this chemoselective transformation, however, sustainable catalyst synthesis requires optimal utilisation of these scarce elements. Here, we report Au catalytic systems based on the deposition of isolated Au sites on different morphologies of ceria in which different surface facets of the support are exposed. Through tailoring the support morphology and from extensive catalyst characterisation, it is shown that the exposed facet is critical for controlling the formation (or not) of isolated Au sites. Both the 110 and 111 facets are capable of this feat, yielding single-atom sites for rod, octahedron, and polyhedron morphologies. In contrast, the 100 facet is not, resulting in Au nanoparticles on cubic ceria. This dictation over Au species is critical to benzyl alcohol oxidation capacity at mild conditions and in the absence of a soluble base, with only single-atom catalyst (SAC) systems demonstrating activity. Furthermore, the exposed surface facet also governs the degree of surface oxygen vacancies, which is critical to catalyst activity due to their control over substrate adsorption strength, as revealed through T_1/T_2 NMR relaxation measurements.

Introduction

The chemoselective transformation of alcohols to their carbonyl derivatives represents a key industrial process that has historically relied on stoichiometric reagents. Thus, highly active and selective oxidation catalysts are prime candidates for the transition to the sustainable production of aldehydes. Industrially important aromatic aldehydes find diverse applications spanning pharmaceuticals, fine chemicals, and the food and fragrances industries,[1] for example; benzaldehyde, which is used in the production of ephedrine, a central nervous system stimulant,[2] malachite green, a dye and an agricultural antimicrobial,[3] and used directly due to its characteristic almond-like odour in the food industry.[4] Conventional production routes from alcohols typically employ stoichiometric oxidants, such as permanganates and chromates, e.g. $KMnO_4$, $K_2Cr_2O_7$ and $Na_2Cr_2O_7$.[5] Their use, however, is plagued by their toxicity and generation of large volumes of aqueous waste.

Heterogeneous catalytic systems for selective oxidation (selox) of alcohols have, in general, focused on platinum group and noble metals as the catalytic species, in particular the use of Pt,[6] Pd,[7] and Au.[8] While the use of Pt and Pd can afford a high catalytic activity, even under base-free mild conditions, the effectiveness, in the case of Pt especially, is quickly diminished through the propensity for unwanted side reactions.[6b,9] Benchmarked against Pd and Pt catalysts, Au systems can show exceptionally high selectivity to aldehyde,[8a] although the addition of base or use of high O_2 pressures are commonplace.[10] CeO_2 has been shown to overcome this requirement of an auxiliary, but only at elevated temperatures and high catalyst:substrate ratio, with the addition of soluble base still required when reaction temperatures are dropped to 50 °C.[11] The use of a solid base as the support is one option to circumvent the need for the additional soluble base while maintaining high conversion and selectivity, albeit at 120 °C.[12] The impact of Au particle size is also critical, with systems produced using hydrotalcite, a layered double hydroxide solid base, as a support material, suggesting smaller nanoparticles are preferable,[12] with TOFs decreasing from 800 h^{-1} to 200 h^{-1} as sizes increased from 2.1 to 12 nm. However, when employing a solid base, the preparation route is critical, with entrained residual soluble base a common issue when employing bases such as NaOH for hydrotalcite production,[13] which in itself can mask the true efficacy of the solid base.[8b]

[a] X. Zhou, A. Mavridis, C. Drivas, C. D'Agostino, C. M. A. Parlett
Department of Chemical Engineering, University of Manchester, Manchester M13 9PL, UK
E-mail: christopher.parlett@manchester.ac.uk

[b] X. Zhou, C. Drivas, C. M. A. Parlett
UK Catalysis Hub, Rutherford Appleton Laboratory, Oxfordshire, OX11 0FA, UK

[c] M. A. Isaacs
HarwellXPS, Rutherford Appleton Labs, Oxfordshire, OX16 0FA, UK

[d] M. A. Isaacs
Department of Chemistry, University College London, London WC1H 0AJ, UK

[e] C. D'Agostino
Dipartimento di Ingegneria Civile, Chimica, Ambientale e dei Materiali (DICAM), Alma Mater Studiorum – Università di Bologna, Via Terracini, 28, 40131 Bologna, Italy

[f] C. M. A. Parlett
University of Manchester at Harwell, Diamond Light Source, Oxfordshire OX11 0DE, UK

Supporting information for this article is available on the WWW under https://doi.org/10.1002/cctc.202301673

However, even at the size range of a couple of nanometres, the utilisation of the metal is suboptimal, with a significant proportion within the bulk of the particle. This issue is further compounded when employing precious metals, given their high cost. In 2011, Zhang coined the term 'single-atom catalyst (SAC)' in a report on the work developing isolated Pt atoms anchored on the surface of FeOx nanocrystals.[14] However, it should also be highlighted that previous reports had identified isolated metal sites as catalytic materials for alcohol oxidations.[15] This approach in producing isolated metal sites represents optimal atomic utilisation and interfacial site generation, which leads to excellent activity. This approach has been expanded to Au-doped ceria, to produce Au_1/CeO_2, which has been shown to be a highly active and stable catalyst for the selective oxidation of alcohol, with turnover frequencies (TOFs) reaching 3036 h^{-1} when screened at 150 °C and 5 bar of O_2.[16] Ceria has also shown promise as a catalyst support in single atom catalysis at elevated temperatures,[17] with the exposure of different surfaces playing a critical role. For example, Pt single atoms can be formed on both rod and octahedron ceria surfaces with dramatic catalytic performance for CO oxidation.[18] In contrast, the formation of SAC of Pd demonstrates a preference towards rod morphology, with nanoparticle resulting when octahedron morphology was employed, albeit with the latter showing higher CH_4 catalytic oxidation performance.[19] SAC of Pd have also been produced on CeO_2(100) facets, which have shown higher selectivity for the catalytic N-alkylation of aniline than Pd clusters on CeO_2(111).[20] Finally, while the impact of ceria morphology on Au nanoparticle catalysts has also been investigated,[21] analogous studies in SAC of gold remain largely unexplored.

To investigate Au_1/CeO_2 systems further, including providing insight into the potential impact of exposed ceria surface facets on the alcohol oxidation performance, SAC of Au deposited on a range of different morphology ceria supports have been produced via the facile adsorption method. CeO_2 with a range of morphologies, i.e., rod (CeO_2-R), cubic (CeO_2-C), octahedron (CeO_2-O), and polyhedron (CeO_2-P), in which exposed surfaces comprise predominately of either 100, 110, and 111, or a mixture of, have been used for the production of Au_1/CeO_2 catalysts or Au_n/CeO_2 where Au nanoparticle form. These have been benchmarked for the selective oxidation of benzyl alcohol against a commercial CeO_2 support (CeO_2-Com), with extensive characterisation to evaluate gold dispersion, oxidation state and local environment.

Results and Discussion

Catalyst Support Properties

Ceria support morphologies and average particle sizes are confirmed by TEM, as shown in Figures 1, S1, and S2, revealing well-defined expected morphologies and exposed surface facets based on the corresponding literature.[22] CeO_2-R comprises uniform rods with average particle diameters of 10 ± 1 nm, with both (110) and (100) facets exposed, which were originally reported as those exposed. However, a more detailed analysis shows a degree of (111) facets, consistent with the report of Chen et al.[19] In contrast, CeO_2-C and CeO_2-O present with average particle sizes of 32 ± 20 nm and 21 ± 3 nm, respectively, exposing either (100) or (111) facet exclusively. Similar to CeO2-R, CeO_2-P and CeO_2-Com both exhibit a mixed facet exposed surface nature, with both showing lattice spacing of 0.19 and 0.31 nm, consistent with 110 and 111 facets.

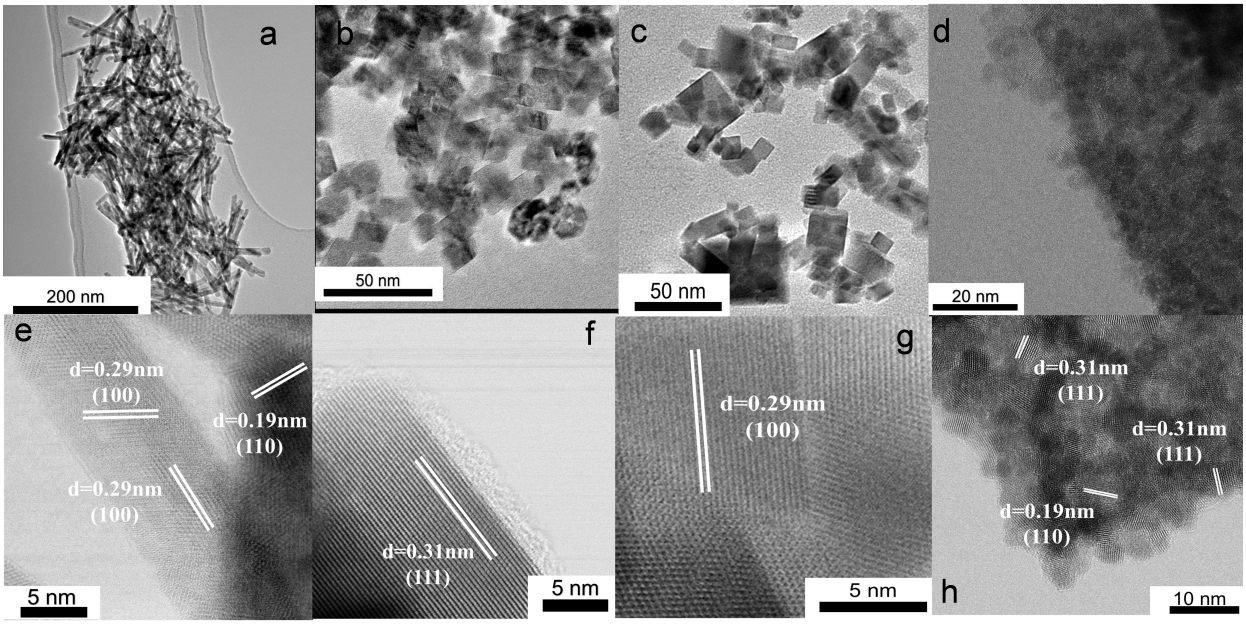

Figure 1. TEM images of (a) CeO_2-R, (b) CeO_2-O, (c) CeO_2-C, (d) CeO_2-P, with high-resolution TEM images shown of (e) CeO_2-R, (f) CeO_2-O, (g) CeO_2-C, and (h) CeO_2-P.

Powder XRD patterns of all CeO_2 supports (Figure 2(a)) confirm the cubic fluorite CeO_2 crystal structure (space group $Fm\bar{3}m$, JCPDS 01–089-8436), with diffraction peaks at $2\theta = 28.7°$, 33.3°, 47.8°, 56.8°, 59.6°, 69.6°, ascribe to the (111), (200), (220), (311), (222), (400) spacings. Furthermore, no impurity or precursor peaks are observed, confirming the uniform CeO_2 nature of all catalyst support morphologies. Scherrer volume averaged crystallite sizes (Table 1) from different peaks for CeO_2-O and CeO_2-C are in good agreement with each other, and the average particle sizes from TEM analysis, which suggests a monocrystalline structure. In a similar manner, the volume averaged crystallite sizes of CeO_2-R reveal a good agreement, irrespective of which refraction peak they are calculated from, with sizes aligning with the average rod diameter. This suggests that the rod morphology comprises a polycrystalline configuration in which crystals join in a linear fashion. Likewise, both CeO_2-P and CeO_2-Com are polycrystalline, as confirmed by the HR-TEM images, with the commercial ceria exhibiting the smallest crystallite sizes. N_2 adsorption-desorption isotherms are shown in Figure 2b, with corresponding BET surface areas reported in Table 1. These exhibit a type II or IV nature with an absence of microporosity and only interparticle pores present, as confirmed by TEM from the absence of internal mesoporosity.

The chemical nature of the ceria supports was evaluated by X-ray photoelectron spectroscopy (XPS), specifically to probe the level of oxygen defects evaluated by the proportion of Ce^{3+}. Ce 3d spectra of the five supports are shown in Figures 3 and S3, with data acquisition length minimised to overcome potential photoreduction.[23] While spectra of CeO_2 are complex, comprising multiple peaks arising from final state effects, coupling of the peaks, i.e., v_0, v', u_0, and u', assigned to Ce^{3+}, and v, v'', v''', u, u' and u''', assigned to the Ce^{4+}, as shown in Figure 3(a),[24] allows surface proportion of Ce^{3+} species to be calculated, which are illustrated in Figure 3(b). The presence of Ce^{3+} is directly related to the presence of missing oxygen atoms at the ceria surface. Their removal leaves surplus electrons localised at the ceria atom within empty f-orbitals, resulting in a valency change (Ce^{3+}/Ce^{4+} redox) per vacancy. This phenomenon can be associated with the reversible formation of oxygen vacancies on CeO_2, and thus, the detection of Ce^{3+} is proportional to oxygen defects at the surface.[25] The three supports exhibiting multifaceted surface terminations, i.e., CeO_2-R, CeO_2-P, CeO_2-Com, show a higher proportion of surface Ce^{3+} relative to the 111 faceted CeO_2-O and 100 facetted CeO_2-C, which suggested a preference for oxygen vacancies over the 110 facets of ceria.[26] The presence of these surface defects, i.e. oxygen vacancies, is critical to the success of the catalyst synthesis through the attraction of anionic Au species present in solution during the facile adsorption protocol, which are prone to anchor at these sites,[27] at least initially during the synthesis, and which are present in levels in excess of the targeted Au loading. Calculations have revealed that the energy of formation for anion vacancies over different CeO_2 surfaces

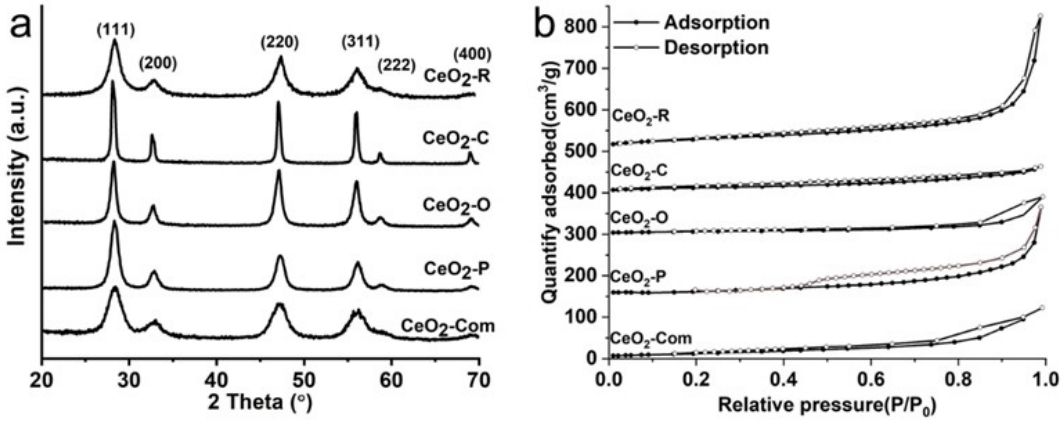

Figure 2. (a) Stacked powder XRD patterns of ceria supports, and (b) stacked N_2 adsorption-desorption isotherms of ceria supports, with CeO_2-R offset by 500 $cm^3 g^{-1}$, CeO_2-C offset by 400 $cm^3 g^{-1}$, CeO_2-O offset by 300 $cm^3 g^{-1}$ and CeO_2-P offset by 150 $cm^3 g^{-1}$.

Table 1. Structural properties and the textural properties of the ceria support.

Sample	Exposed facet [a]	Surface area($(m^2 g^{-1})$ [b])	Crystal size (111)/nm[c]	Crystal size (200)/nm[c]	Crystal size (220)/nm[c]
CeO_2-C	(100)	23	27	25	28
CeO_2-O	(111)	47	17	15	16
CeO_2-R	(100) (110)	103	7	7	8
CeO_2-P	(110) (111)	58	13	13	12
CeO_2-Com	(110) (111)	43	5	5	5

a) Measured by TEM. b) S_{BET} = surface area, measured by the Brunauer-Emmett-Teller (BET) Method. c) Calculated from the corresponding diffraction peak using the Scherrer equation.

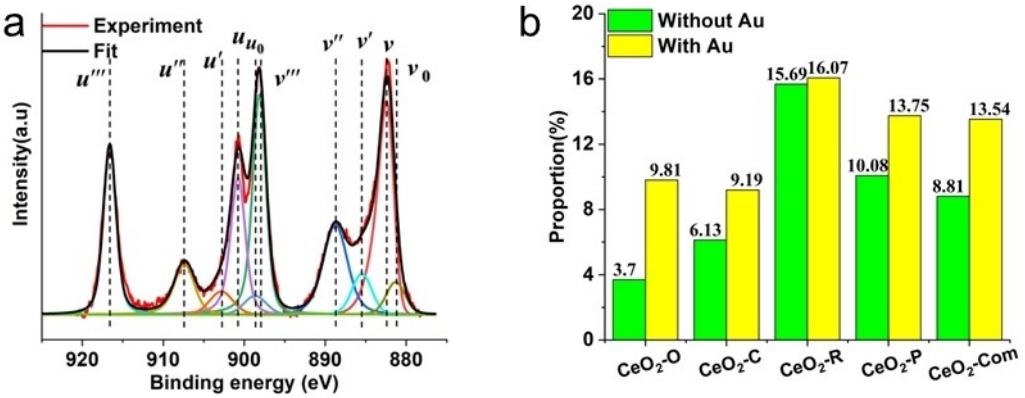

Figure 3. (a) Representative Ce 3d X-ray photoelectron spectra of CeO_2 (CeO_2-R shown), and (b) proportion of surface Ce^{3+} present in parent ceria supports and corresponding catalysts.

varies as follows 110 < 100 < 111,[28] i.e. oxygen vacancies are formed more readily on the (110) planes, consistent with the higher concentrations present in CeO_2-R, CeO_2-P, and CeO_2-Com, which may provide a route to increase Au loadings.

Au-Doped CeO_2 SACs Characterisation

Gold catalytic sites were introduced to the five ceria support morphologies via a facile deposition route with a nominal loading of 0.1 wt.%, yielding a series of CeO_2-based Au SAC (Au_1/CeO_2-X).[14] Au loadings are confirmed by X-ray fluorescence spectroscopy (XRF) and microwave plasma atomic emission spectroscopy (MP-AES), with values listed in Table S1 confirming excellent agreement between the desired and actual loadings. Powder XRD (Figure S4) reveals both the absence of new peaks corresponding to Au, indicative of high Au dispersion, and the retention of the CeO_2 fluorite crystalline phase, with no impact on average crystallite size (Table S1).

Atomic dispersion of Au was first confirmed by high-resolution high angle annular dark field scanning transmission electron microscopy (HAADF-STEM),[29] based on Z contrast imaging.[30] Representative images are shown in Figures 4 (a–c) and S5–7, for which analysis across a range of magnification confirmed the absence of Au clusters or nanoparticles for Au_1/CeO_2-R, Au_1/CeO_2-P, Au_1/CeO_2-O, and Au_1/CeO_2-Com. Furthermore, at high magnification, isolated single Au atoms, identified as single bright spots, dispersed on the CeO_2 surface are clearly observed, confirmed from intensity mapping and image modelling, thus confirming the SAC nature of these four catalysts. Electron micrograph simulations, shown in Figures 4 (d–f) and S8, confirm that isolated Au single-sites on CeO_2 are detectable through a clear enhancement in HAADF-STEM intensity when Au is located on the Ce atom column, which is true for thickness up to ~10 nm, thus confirming that identifying these species within the CeO_2-R, CeO_2-Com, and CeO_2-P, should be straightforward. This location reflects at least a partial migration from the initial adsorption site, i.e. oxygen vacancies. The stabilisation of these isolated sites is attributed to the presence of surface Ce defect sites, serving as anchor sites to stabilise atomic Au and prevent it from aggregating.[31] In contrast, the cubic morphology of CeO_2 gives rise to nanoparticles of Au (Au_n/CeO_2-C), confirmed by lattice spacing of 0.23 nm, which corresponds to Au (111) of metallic Au, as shown in Figure 5. Furthermore, no isolated Au sites are observed, although this could be due to the larger crystallite size of the cubic morphology, impacting the ability of HAADF-STEM to identify them. The diameter of these Au nanoparticles is in the order of 3–4 nm, i.e. at the crystallite size detection limit of Cu Kα powder XRD. Thus, defect sites on the 100 facets of CeO_2 are clearly unable to stabilise isolated Au sites, with deposition followed by migration and sintering.

Au 4f X-ray photoelectron spectra of the five catalysts reveal a distinct difference in the oxidation state of the isolated Au sites (Au_1/CeO_2-R, Au_1/CeO_2-P, Au_1/CeO_2-O, and Au_1/CeO_2-Com) compared to the Au nanoparticles (Au_n/CeO_2-C), as indicated in Figure 6. The high energy resolution spectra show a distinct binding-energy shift of the Au 4f peaks, with a higher oxidation Au species present for rod, octahedron, polyhedron, or commercial systems, compared to Au present on the cube morphology. Peak fitting, via non-linear least squares, confirms Au to be present as a single identical species, assigned as cationic Au(I), with a $4f_{7/2}$ binding energy of 84.6 ± 0.2 eV within Au_1/CeO_2-R, Au_1/CeO_2-P, Au_1/CeO_2-O, and Au_1/CeO_2-Com. In contrast, Au_n/CeO_2-C shows a peak shift to 83.4 eV, which we attribute to metallic gold (Au^0), although again, it only presents as a single Au species. This represents a slight shift relative to the bulk Au value of 84.0 eV, reflecting the nanoparticulate nature, which give rise to binging energy shifts due to electron transfer, size effects, and surface structure.[32] Furthermore, Au deposition in all catalysts results in an increase in Ce^{3+} content, indicated in Figure 3. This concurs with previous studies and has been attributed to electron donation from the noble metal to the Ce^{4+} sites.[33]

To further probe the electronic state of the Au sites and shed light on the local environment surrounding the Au-isolated sites, X-ray absorption spectroscopy (XAS) was conducted. Au L_3-edge X-ray absorption near-edge structure (XANES) spectra of Au foil, Au $(OH)_3$, and the Au_1/CeO_2 catalysts are presented in Figure 7a. The XANES spectra are consistent

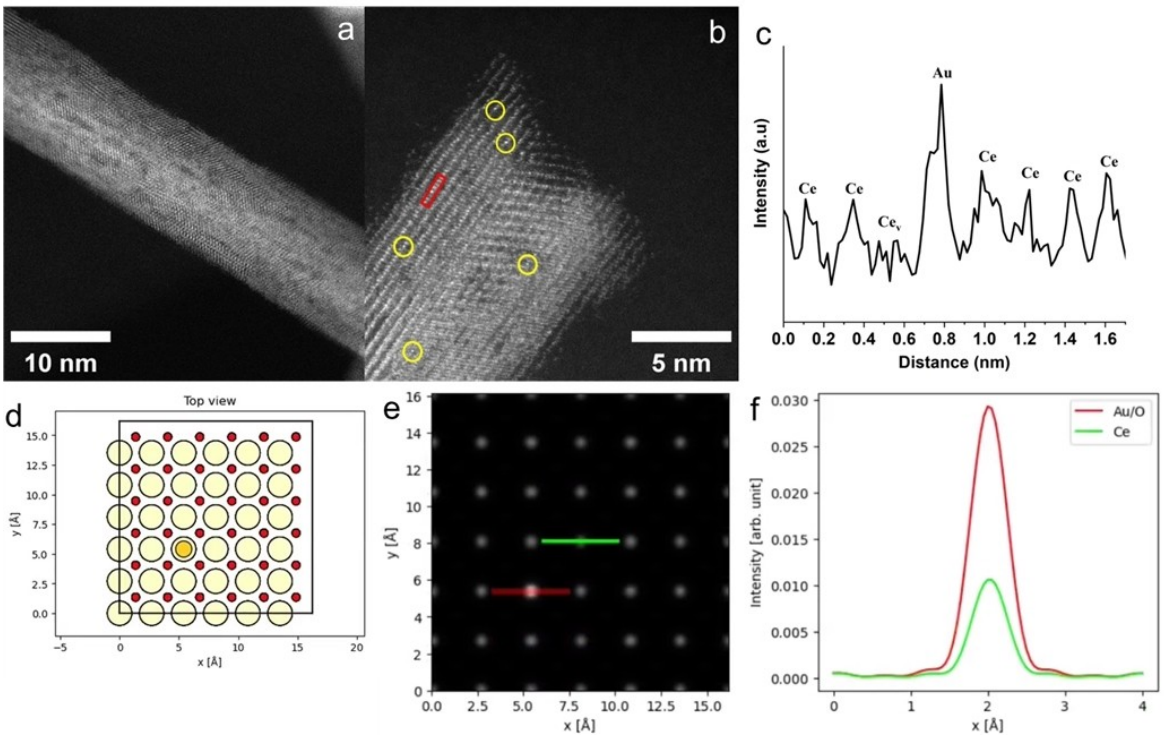

Figure 4. (a) low-magnification of HAADF-STEM images Au_1/CeO_2-R (b) high-magnification of HAADF-STEM images Au_1/CeO_2-R (Au single-atoms highlighted with yellow circles), (c) normalized intensity profiles from (b) indicated by the red box, (d) atomic structure of Au_1/CeO_2 built with Atomic Simulation Environment for image modelling, (e) annular dark field (ADF)-STEM simulation image of Au_1/CeO_2 from (d), and (f) line profile from Au single-site in Au_1/CeO_2 ADF-STEM simulation in (e).

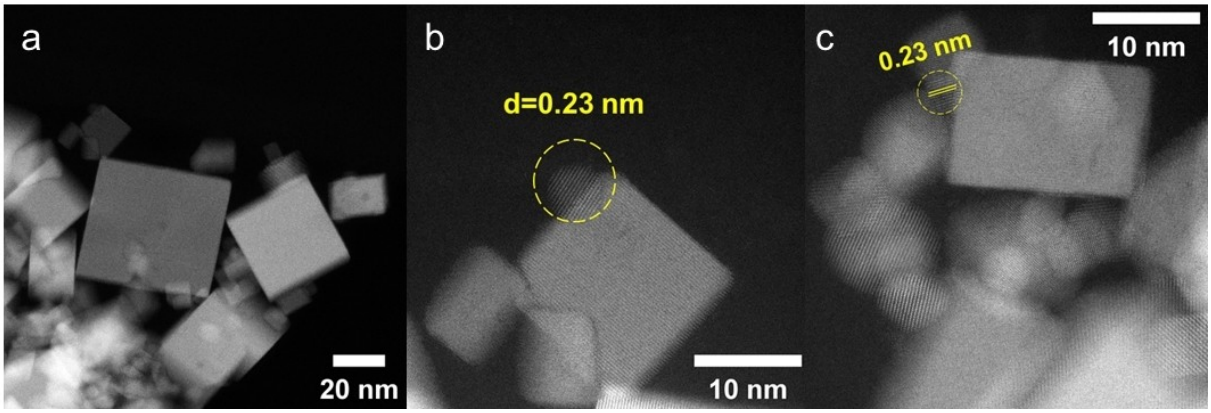

Figure 5. (a) low-magnification of HAADF-STEM images Au_n/CeO_2-C, (b–c) high-magnification of HAADF-STEM images Au_n/CeO_2-Cubic with Au NPs highlighted by yellow circles.

with XPS, confirming the metallic nature of the Au species in Au_n/CeO_2-C, i.e. the spectra match that of Au foil, while Au_1/CeO_2-R, Au_1/CeO_2-P, Au_1/CeO_2-O, and Au_1/CeO_2-Com are clearly not metallic. For the 4 SAC species, the shift in edge and increase in white line intensity are consistent with an increase in oxidation state.[34] EXAFS region fitting, reported in Figures 7b, S9 and Table S2, provides further insight into the Au active site nature. For Au_1/CeO_2-R, Au_1/CeO_2-P, Au_1/CeO_2-O, and Au_1/CeO_2-Com, the dominant scatter is at a bond length of ~1.97 Å,[35] which corresponds to oxygen in the first coordination shell. In all but Au_1/CeO_2-O, the presence of both metallic Au and bulk oxide phases are ruled out via the absence of corresponding first and second shell scatters of these, respectively. The scatters at further distances being attributed to Ce in the second shell from the support, i.e. a Ce scatter at ~3.28 Å, which is an increase in distance compared to the expected value for Au in the second shell for Au_2O_3 (3.049 Å),[36] due to the greater atomic radii of Ce vs Au. Thus, consistent with solely isolated Au sites being present in Au_1/CeO_2-R, Au_1/CeO_2-P, and Au_1/CeO_2-Com. For Au_1/CeO_2-O, fitting results improve significantly with the inclusions of a scatter at 2.87 Å, which is consistent with the presence of metallic Au. This species is only

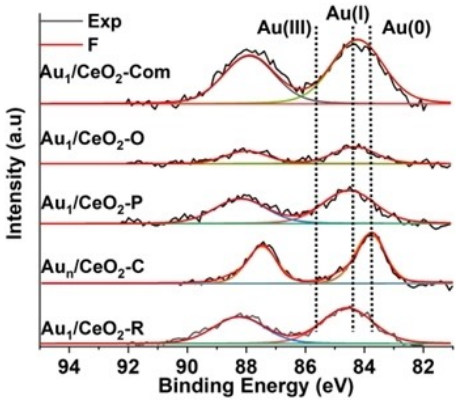

Figure 6. Stacked X-ray photoelectron spectra of Au_1/CeO_2-X catalysts.

present in a small degree and with an average coordination number (CN) of ~6.2, i.e. present as small clusters of Au. The inclusion of this second Au site agrees with the slight reduction in white line intensity observed by XANES. For Au_n/CeO_2-C, the first shell is observed at ~2.84 Å, confirming the presence of metallic Au nanoparticles, with an average CN of ~11.5.

Given the comparable Au deposition protocol applied, the reason for the apparent inability of ceria cubes to support isolated Au sites is an interesting one. Theoretical studies have revealed extraction of oxygen from different CeO_2 facets reveals a more facile removal from (110) vs (111),[37] which can account for polyhedron, commercial, with (110) and (111) exposed, and ceria nanorods, with (110) and (100) exposed, proving to be superior supports for anchoring isolated cationic Au gold species, based on XPS and XAS analysis, compared to the octahedron support. With respect to the cube support and its inability to stabilise Au single-sites, this may reflect the reduced stability of the CeO_2 (100) plane,[38] which may lead to restructuring,[39] or due to greater mobility of surface atoms, even at room temperature,[40] which individually or combined lead to subsequent Au sintering. Furthermore, the inherently lower Ce^{3+} content relative to the rods, which also displays the (100) facet, justifies the absence of NPs in Au_1/CeO_2-R. Identical observations have been reported for both Pd and Pt,[17a,19] suggesting this is a common phenomenon. This can also be expanded to Au nanoparticles on 100 vs 111 CeO_2 facets, with 111 inhibiting sintering due to its great stability.[41]

Alcohol Selox Oxidation

The catalytic performance of the single-atom and nanoparticulate catalysts were evaluated for the selective oxidation of benzyl alcohol to benzaldehyde under base-free conditions and with an Alcohol:Au molar ratio of 4000 at 90 °C. Reaction profiles under static air and flowing O_2 are depicted in Figures S10 and 8 (a and b), respectively, with activities, selectivity and mass balances reported in Tables S3 and S4. Blank reactions, conducted using bare ceria supports, showed negligible conversion (< 1 %) after 6 h, while mass balances for all studies are above 95 %, confirming reactant/product evaporation or adsorption are negligible.

Of the five catalysts, Au_1/CeO_2-R exhibits both the highest conversion and initial activity (TOFs) (Figure 8 (c)), the latter evaluated prior to the onset of on-stream deactivation observed for all catalytically active materials. Comparing performance under static air and flowing O_2 reveals the critical role of O_2 in maintaining catalytic performance and diminishing the impact of catalyst deactivation. Given the obvious positive impact of O_2, it raises the question of the origin of this, with its potential impact being either replenishment of active oxygen species on the CeO_2 surface, although not at the rate at which they are consumed, especially at the latter stages of the reaction,[11] or that it aids in stabilising the surface Au^+ single-sites, which could promote aldehyde desorption. Furthermore, the presence of O_2 flowing through the reaction liquid could also inhibit the reduction of the Ce^{4+}.[42] Given that TOFs are evaluated before apparent catalysts deactivation, the values for the two conditions are within error, while selectivity towards benzaldehyde

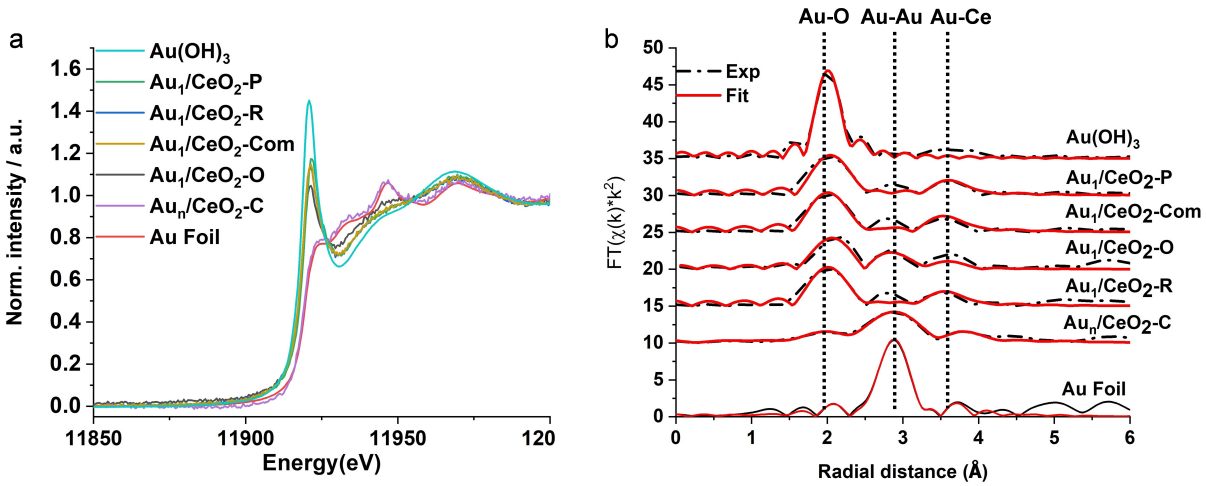

Figure 7. (a) Au L_3 XANES spectra for Au_1/CeO_2-X catalysts and Au_n/CeO_2-C catalysts, Au foil, and Au $(OH)_3$, and (b) phase corrected EXAFS *R*-space magnitude and experiment fit for Au_1/CeO_2-X catalysts and Au_n/CeO_2-C catalysts, Au foil, and Au $(OH)_3$.

is greater than 95%. The catalytic performance of the SAC catalysts follows the order of Rods > Polyhedron > Commercial ≫ Octahedron, with TOFs showing a strong correlation to Ce^{3+} concentration in the final catalyst, as illustrated in Figure 8 (d). Given the equal Au loadings and nature in all active systems, this is consistent with an active site comprising both an Au single-site and oxygen vacancy in the immediate vicinity of each other, which has been proposed by Lei et al. for nanorods systems via the combination of DFT and experiential studies.[43] Thus, this active site configuration can be expanded to other morphologies and surface facets of ceria as a generic species responsible for alcohol oxidations over Au SAC sites on CeO_2. The significant reduction in activity for the octahedron-based system, relative to the other Au_1/CeO_2-X catalysts, is proposed to reflect the difference in the facet the Au SAC sites are supported on rather than the presence of Au NPs. The latter having been identified solely by XAS (discussed above), with the very slight difference in the XANES region reflecting a very minor contribution of NPs to the overall Au species nature, i.e. SAC are the predominant species. It can thus be concluded that the exposed crystal facet of CeO_2 plays a decisive role in the catalytic processes. This change will impact the precise nature of the cooperating Au SAC and oxygen vacancies active sites while also impacting the potential for oxygen donation, i.e. reflecting the greater preference of (110) vs (111) to donate oxygen.[37,39] Consistent with the superior performance of polyhedron and commercial systems, which display (110) and (111) facets, and nanorods, which comprise (110) and (100) facets. In contrast, the Au_n/CeO_2-C are shown to be inactive under both static and flow conditions. This is a direct consequence of the elimination of the dual species active site present within the other catalytic systems, which arises from Au presiding solely as Au NPs. Furthermore, this absence of activity strengthens the case for the pivotal role of soluble base during alcohol oxidation over Au NPs,[8b] under mild conditions, and the critical role of catalyst support synthesis conditions.[13] To further confirm isolated Au sites over Au NPs as the catalytic species responsible, pre-reduction under H_2 at 400 °C of Au_1/CeO_2-R was conducted in order to facilitate the metamorphosis of isolated Au into small metallic NPs (Au_n/CeO_2-R-reduced), confirmed by XPS and TEM (Figure S11). The reduction protocol completely killed the intrinsic activity of Au_1/CeO_2-R, resulting in the performance of Au_n/CeO_2-R-reduced mirroring that of AuNP/CeO_2-C.

The heterogeneous nature of the catalysts was confirmed through a hot filtration test performed using the optimal Au_1/CeO_2-R catalyst (Figure S12). Removal of the catalyst after 1 h confirmed the absence of leached active species, with the reaction halted upon catalyst removal. Moreover, catalyst stability was also confirmed for this most active system, shown

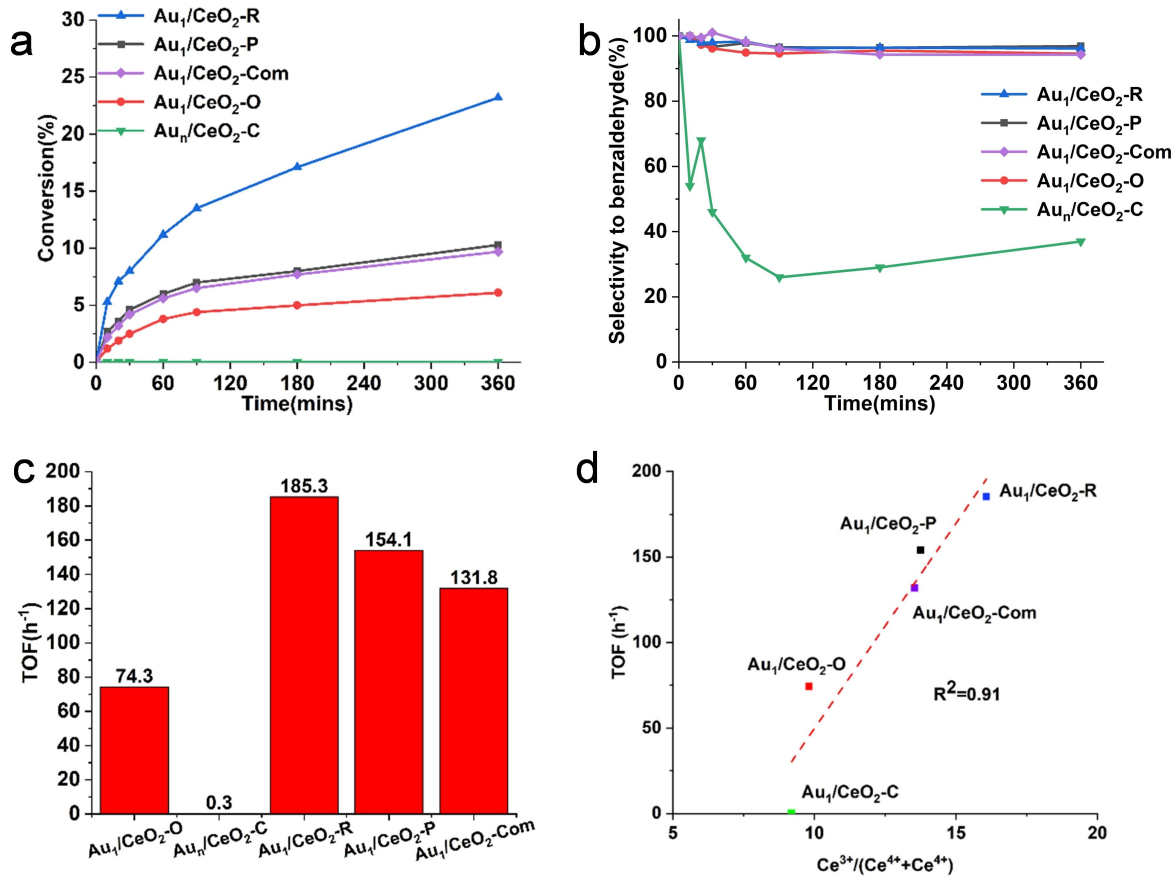

Figure 8. (a) Benzyl alcohol selox reaction profiles over Au_1/CeO_2-X and Au_n/CeO_2-C catalysts (reaction conditions: 1 mmol benzyl alcohol, 10 cm^3 toluene, 50 mg catalyst, at 90 °C under flowing O_2 (1 bar, 10 $cm^3 min^{-1}$)), (b) benzaldehyde selectivity profiles, (c) TOFs calculated over the initial 0.33 h, and (d) direct correlation between catalyst Ce^{3+} content and activity.

in Figure 9, with conversion dropping slightly over the four runs but selectivity remaining high. This unwavering selectivity is indicative of a common active site across all cycles, i.e. a stable Au SAC species. At the same time, the minimal drop in conversion may reflect a slight degree of sintering. However, this is expected to be minor based on the retainment of activity and inactivity of Au nanoparticles under these conditions. The recycled catalyst was reactivated via thermal treatment under air at 400 °C for 30 mins to remove any strongly bound hydrocarbon species, with adsorbed species identified by attenuated total reflection infrared spectroscopy (ATR-IR) (Figure S13). It is pointed out that the higher conversions, reaching ~70%, reflect the reduced substrate:Au ratio of 1000, although this is still significantly higher than that employed by others.[11]

NMR Relaxation

To further study the influence of support morphology with the aim of further illuminating the origin of the difference in catalyst activity and potential reasons for deactivation, NMR relaxation measurements have been used to probe relative adsorption strengths of the reactant, product, and solvent, alongside conventional probes for hydrophilicity (water) and hydrophobicity (*n*-octane).[44] Through a comparison of T_1/T_2, the relative interaction strengths between adsorbate and adsorbent can be elucidated, with positive correlations between Au particle size and activity previously reported for both 1,4-butanediol and glycerol oxidation over Au/TiO_2 catalysts.[44c,45] Representative two-dimensional T_1/T_2 plots of benzyl alcohol adsorption are shown in Figure 10, clearly showing two types of interactions arising for benzyl alcohol adsorption, which present as two peaks in the plots, a major peak (peak 1) associated to the aromatic ring and a second minor peak (peak 2) associated to the alcohol functionality. This assignment is supported by previous work on NMR relaxation studies on alcohols in porous supports.[46] The intensity of these peaks is directly proportional to the number of protons belonging to the chemical functionality associated with each peak, with the aromatic ring exhibiting a much higher intensity compared to the hydroxyl group of the alcohol, with peak area volumes in good agreement between the measured volume ratio and the theoretical ratio, i.e. 5:1. These reflect the interaction of the adsorbate through either the aromatic ring or the alcohol functional group. Likewise, benzaldehyde also demonstrates two types of interactions, this time with the second resulting from the proton on the carbonyl group, with the assignment consistent with previous reports.[46] In both cases, the interaction with the oxygen-containing functional group (peak 2) is significantly stronger, reflected in the higher T_1/T_2 value.[47] Again, for benzaldehyde, the peak volume ratio is in good agreement with the expected value. In contrast, toluene (solvent), water, and *n*-octane show a single interaction, i.e. a single peak, with water significantly more strongly interacting than toluene or *n*-octane, which indicates a hydrophilic nature of the catalyst surface (Figure S14).

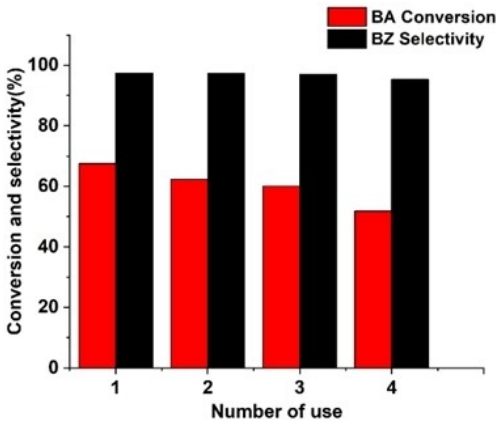

Figure 9. Benzyl alcohol conversion and benzaldehyde selectivity over four cycles for Au_1/CeO_2-R (initial reaction conditions: 1 mmol benzyl alcohol, 10 cm^3 toluene, 200 mg catalyst, at 90 °C under flowing O_2 (1 bar, 10 $cm^3 min^{-1}$)). Reaction conditions are adjusted to maintain alcohol:Au of 1000 and consistent substrate concentrations of all cycles.

Computational studies have proposed that Ce^{3+} is critical in benzyl alcohol oxidation, acting as the site for alcohol adsorption,[43] which is consistent with the catalyst data reported here (Figure 8 (d)). The identification of the Ce^{3+} adsorption site is further verified experimentally here from the strong positive correlation between the T_1/T_2 ratio of the alcohol functional group and the Ce^{3+} content, as shown in Figure 11(a). This strong correlation is only observed for the SACs, and while a similar positive correlation for the support is also observed, the correlation is significantly weaker (Figure S14a). Furthermore, the correlation arises only for the alcohol functional group, with no correlation observed between the aromatic functionality and the catalyst (Figure S14b), thus confirming that the critical interaction is between the alcohol functional group and the Ce^{3+} sites. In contrast, there is no effect of Ce^{3+} content on the adsorption strength of benzaldehyde (Figure 11(b)), which binds considerably more weakly but uniformly across all of the catalysts. This is a critical aspect, with this reduced adsorption strength (relative to the alcohol) ruling out competitive adsorption of the product (i.e. poisoning) as the route of deactivation, as observed in the catalytic studies discussed above. Moreover, increasing Ce^{3+} content is shown to decrease the interaction strength of the catalyst with the solvent (Figure S14c), thus reducing the potential of competitive adsorption of the solvent, with an identical trend seen for *n*-octane, indicating that an increasing Ce^{3+} content results in more hydrophilic surfaces (consistent with the positive correlation for water) (Figure S14).

Conclusions

The critical role that ceria morphology can impart on both active site stabilisation, through the generation of either single-atom sites or metallic nanoparticles, and catalyst activity has been demonstrated through a diverse range of gold functionalised ceria supports and their application for benzyl alcohol selox to benzaldehyde. Through tuning ceria support morphol-

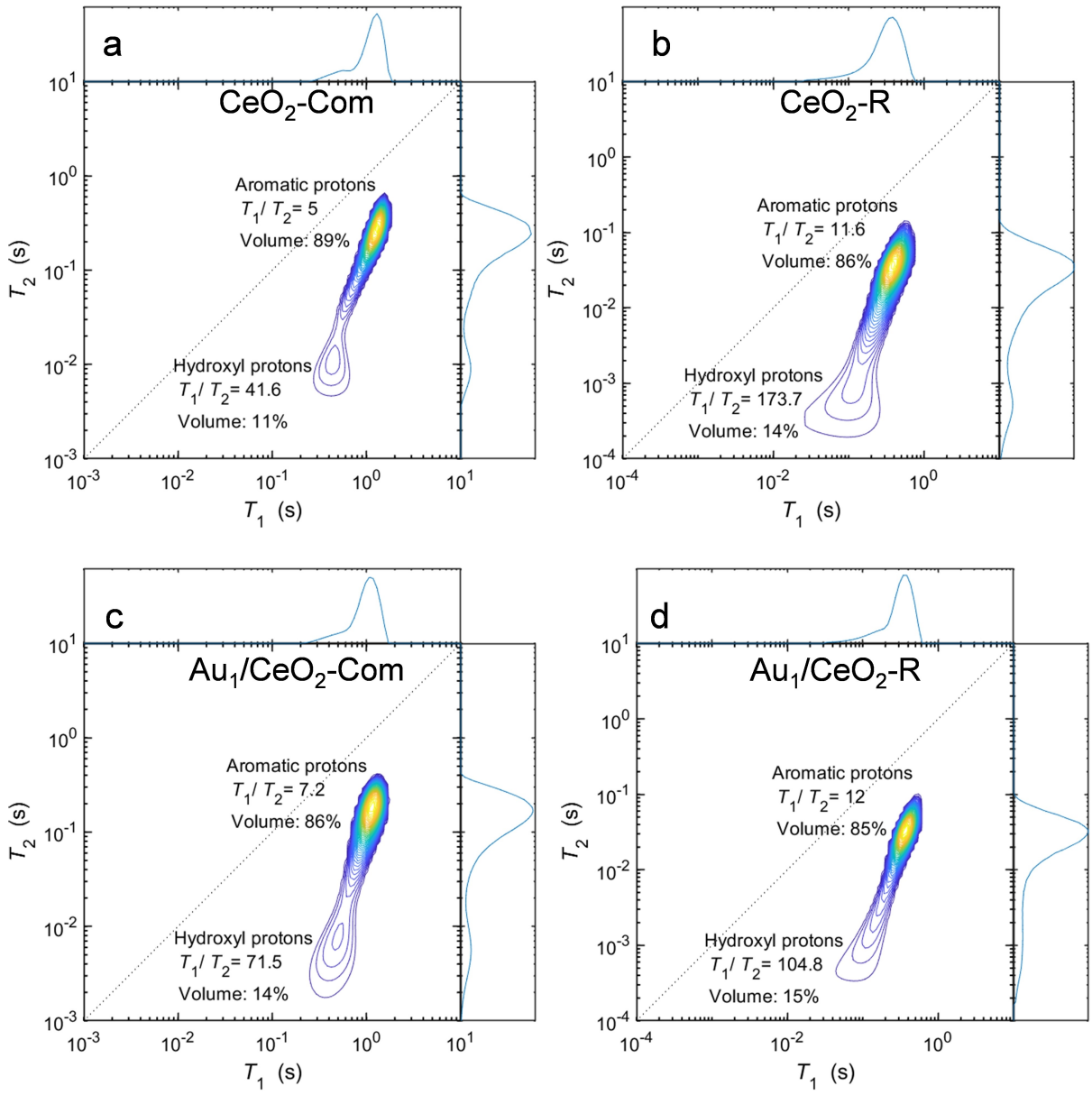

Figure 10. Representative T_1/T_2 ratio for benzyl alcohol adsorption on (a) CeO_2-Com, (b) CeO_2-R, (c) Au_1/CeO_2-Com, and (d) Au_1/CeO_2-R.

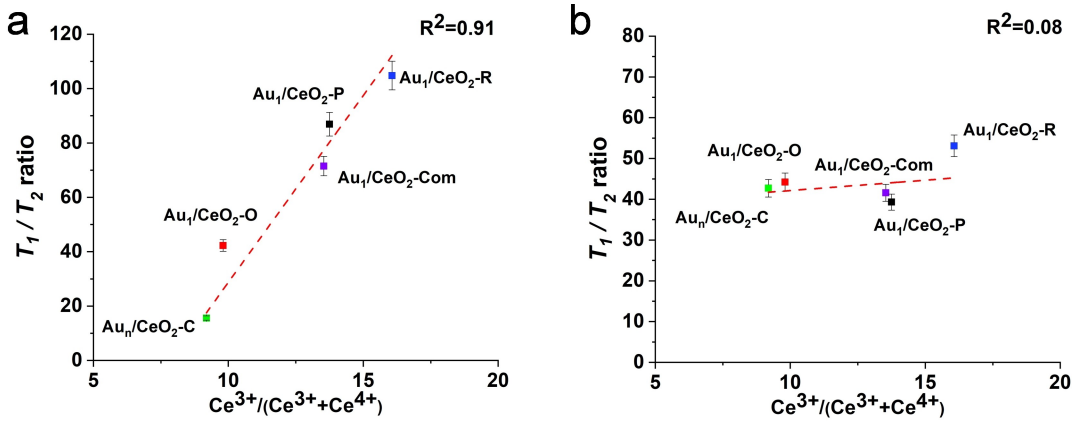

Figure 11. Correlation between T_1/T_2 ratios and catalyst Ce^{3+} content for (a) benzyl alcohol, and (b) benzaldehyde adsorption on Au_1/CeO_2-X and Au_n/CeO_2-C catalytic materials (T_1/T_2 evaluated from interaction with alcohol and carbonyl functional group).

ogy, it has been possible to control the exposed facets, with 100, 110, and 111 surfaces exposed either solely or a combination. A cube morphology exposes solely the 100 facet, which stabilises Au as nanoparticles, whereas single-atom Au sites are present when the 110 or 111 facet is exposed. For example, rod, polyhedron, and commercial ceria, which present a combination of either 110 and 100 (rods) or 110 and 111 (polyhedron and commercial), and octahedron, which exhibits the 111 facet only, all result in isolated Au sites, yielding SAC species. This control over Au speciation is critical to the result catalytic activity, with SAC demonstrating the capacity of base-free alcohol oxidation under mild conditions while Au nanoparticles are inactive. Furthermore, ceria support morphology plays a critical role in surface oxygen vacancy formation, which is shown to be a critical parameter to the resulting catalytic activity of the single-atom Au sites due to its governing benzyl alcohol adsorption strength. Thus, Ce^{3+} content is critical in controlling catalyst activity through both Au active species generation and benzyl alcohol adsorption, which occurs preferentially through the alcohol functional group and in close proximity to the Au site, i.e. this dual functionality is critical for efficient catalytic activity. The findings reported here guide the design and optimisation of ceria supported Au single-atom catalysts for effective alcohol selective oxidations, with increasing Ce^{3+} content, initially of the support and subsequently of the catalytic system, an apparent approach to further escalate the resulting catalytic performance. The former through providing routes to higher Au SAC loadings, and the latter to increase benzyl alcohol adsorption, although this interaction may well reach an optimum before maximum Ce^{3+} levels are achieved.

Experiment Sections

Preparation of Ceria Morphologies

All chemicals were of analytical purity.

Ceria Rods

1 dm^3 of cerium (III) nitrate hexahydrate solution (0.1 M) and 700 cm^3 of aqueous sodium hydroxide solution (6 M) were prepared using deionised water. Sodium hydroxide and cerium (III) nitrate solutions were mixed in a 2 dm^3 Teflon bottle at 640 rpm for 0.75 h at room temperature before heating to 95 °C for 24 h. The precipitate was recovered by filtration, washed with deionised water to neutral pH, and then washed with ethanol five times. The solid was dried at 70 °C overnight, yielding yellow powder, which was donated as CeO_2-R.[22c]

Ceria Cubes

1 dm^3 of cerium (III) nitrate hexahydrate solution (0.1 M) and 700 cm^3 of aqueous sodium hydroxide solution (6 M) were prepared using deionised water. Sodium hydroxide and cerium (III) nitrate solutions were mixed in a 2 dm^3 Teflon bottle at 640 rpm for 0.75 h at room temperature. The solution was transferred into a Teflon-lined autoclave and heated to 180 °C for 24 h. The precipitate was recovered by filtration, washed with deionised water to neutral pH, and then washed with ethanol five times. The solid was dried at 70 °C overnight, yielding yellow powder, which was donated as CeO_2-C.[22c]

Ceria Octahedral

0.434 g cerium (III) nitrate hexahydrate was dissolved in 35 cm^3 of aqueous sodium hydroxide solution (0.01 M). After stirring for 1 h at 640 rpm, the solution was transferred into a Teflon-lined autoclave and heated to 180 °C for 12 h. The precipitate was recovered by filtration, washed with deionised water to neutral pH, and then washed with ethanol five times. The solid was dried at 70 °C overnight, yielding yellow powder, which was donated as CeO_2-O.[20]

Ceria Polyhedron

100 cm^3 aqueous cerium nitrate hexahydrate (0.1 M) was added dropwise to 100 cm^3 of aqueous sodium carbonate (0.1 M) solution under vigorous agitation (stirring at 640 rpm) over 3 h at 50 °C, while the pH of the solution was controlled at ca. 8. After vigorously stirring for 3 h and ageing for another 3 h, the resulting precipitate was collected by filtration and washed with deionised water to neutral pH, and then washed with ethanol five times. The recovered solid was dried at 70 °C for 6 h and then calcined at 400 °C for 5 h, yielding a yellow powder, which was donated as CeO_2-P.[16]

Preparation of Catalysts

Single Au atoms were deposited onto the ceria support via the facile absorption (Strong electrostatic adsorption) methodology.[35a] 1 g of CeO_2 support was dispersed in 30 cm^3 deionised water with vigorous stirring. 40 mg Gold (III) chloride trihydrate was dissolved in 100 cm^3 of deionised water, with the required amount added dropwise into the CeO_2 solution under stirring. After continuous stirring at 600 rpm for 2 h and subsequent static ageing for 2 h, the solid was isolated by filtration and washed with deionised water and ethanol. The solid was dried at 60 °C overnight. The synthesised catalyst was denoted as Au_1/CeO_2-X, with X adjusted depending on the ceria support morphology. A commercial CeO_2 (Sigma-Aldrich, surface area 30–40 $m^2 g^{-1}$) was likewise loaded with Au as a benchmark material.

Characterisation of Catalysts

X-ray diffraction patterns were recorded on a Rigaku Miniflex X-ray diffraction (XRD) instrument (Cu Kα1, 45 kV, 2θ from 20–70°, step 0.01°, speed 0.2 s/°) with fixed divergence slits. Nitrogen adsorption-desorption isotherm experiments were conducted at −196 °C on a Quadrasorb SI model SI-20 Quantachrome instrument. Surface areas were calculated using the BET method over the relative pressure range from 0.05 to 0.2, where a linear relationship was observed. Microwave plasma-atomic emission spectroscopy (MP-AES) analysis was performed on an Agilent microwave plasma atomic emission spectrophotometer (4100 MP-AES, Agilent Technologies). The recorded spectral intensity was the mean of 5 replicate readings for each sample. Au calibration standard solutions were recorded at four different wavelengths, 267.595, 242.795, 312.278 and 274.825 nm, with a calibration curve with a linear fit and correlation coefficient value over 0.9998 obtained at 242.795 nm, which was used to determine the actual Au loadings. TEM imaging analysis of all the catalysts was performed using a JEOL electron microscope JEM2100 Plus on TEM mode at an operating voltage at 200 kV with a LaB6 filament with a single tilt holder. Samples were prepared by drop-casting from a dispersion

in menthol onto a copper grid coated with holey carbon. HAADF-STEM images were performed using a JEOL ARM 300CF microscope (probe aberration-corrected) at the electron Physical Science Imaging Centre, Diamond Light Source, with an acceleration voltage of 200 kV. The STEM simulations were performed with AbTEM using the PRISM algorithm and Kirkland potential parameterisation. XPS analysis for the catalysts was performed on a Thermo Fisher Scientific NEXSA spectrometer. The XPS was equipped with a micro-focused monochromatic Al X-ray source (180 W, 400 μm). Data were recorded at pass energies of 50 eV for Au 4 f, O 1 s and Ce 3 d scans with 0.1 eV step size. The samples were measured under a vacuum of 10^{-7} mbar and at room temperature with a charge neutralisation mode. The recorded data were analysed by CasaXPS (version 34 2.3.19PR1.0). The binding energy was calibrated by using C 1 s (284.7 eV). Au L_3 X-ray Absorption Spectroscopy (XAS) measurements of all catalysts were performed on the B18 beamline at the Diamond Light source. A fast-scanning Si (111) double crystal monochromator and the harmonic rejection mirror were used. The 35 mg powder samples were pressed into pellets after mixing with 25 mg Boron nitride. Spectra were collected in fluorescence mode, with Au foil simultaneously collected from a foil placed between I_t and I_{ref} ion chambers. The scanning time for each spectrum was around 15 min, with 4 scans collected, to achieve high signal-to-noise to enable fitting up to a k_{max} of 14. XAS data processing was conducted using the Demeter software package, Athena for XANES analysis and Artemis for EXAFS fitting.[48] All the NMR measurements have been performed on a Spinsolve instrument by Magritek, with a magnetic field strength of 1 Tesla (larmor frequency of 43 MHz for hydrogen nuclei). The ceria powders have been soaked in the selected liquids overnight so that they become saturated. Before the measurements, a filter paper was used to remove the excess liquid, allowing us to probe a thin surface layer adsorbed to the powder surfaces. A standard IR-CPMG pulse sequence was used, as reported previously. A numerical inversion algorithm has been used to process the experimental data to obtain 2D maps with the T_1 and T_2 relaxation time distributions as their axes. The T_1 and T_2 time constants for each of the peaks in the 2D maps can be evaluated by weighted average methods. The average volume fraction of all the peaks representing aromatic hydrogens is 83.3%, and the average volume fraction of peaks representing hydrogens in hydroxyl or formyl groups is 16.9%, consistent with the expected ratio. Attenuated total reflectance infrared spectroscopy (ATR-IR) was performed using a Thermo Nicolet iS 10 Fourier transform infrared spectrometer fitted with a Smart iTR attenuated total reflectance accessory. Spectra were collected as an average of 32 scans with a resolution of 4 cm^{-1}, using air as the background.

Catalysts Screening

Liquid phase catalyst screening was performed using a Radleys Starfish carousel batch reactor. 50 mg catalyst (unless stated otherwise) was added to a reaction mixture of benzyl alcohol (0.108 g), mesitylene (0.1 cm^3) and toluene (10 cm^3) at 90 °C under stirring at sufficient rates (900 rpm), so that bulk diffusion limitations are overcome. Reactions were conducted under air or flowing oxygen (10 $cm^3 min^{-1}$). The solution was heated to the desired temperature, with the catalyst added once the temperature was achieved to initiate the reaction. Reaction aliquots were periodically taken for GC analysis at 0, 0.25, 0.5, 0.75, 1, 1.5, 3 and 6 h. Recycle tests were conducted by scaling up to 200 mg of catalyst for the first cycle and subsequently scaled to the mass of the recovered catalyst. The recovered catalyst was reactivated at 400 °C in air for 0.5 h.

Acknowledgements

UK Catalysis Hub is kindly thanked for the resources and support provided via our membership of the UK Catalysis Hub Consortium and funding by EPSRC grant: EP/R026815/1. C.D.A. would like to acknowledge the EPSRC grant no. EP/V026089/1. The authors acknowledge Diamond Light Source for time on beamlines B18 under proposal SP19850 and ePSIC under proposal MG33779. C.A.M.P. would like to thank the Research Complex for access and support to these facilities and equipment. We would like to thank Gavin Stenning for help on the Rigaku Miniflex benchtop XRD instrument in the Materials Characterisation Laboratory at the ISIS Neutron and Muon Source. The X-ray photoelectron (XPS) data collection was performed at the EPSRC National Facility for XPS ("HarwellXPS"), operated by Cardiff University and UCL, under Contract No. EP/Y023587/1.

Conflict of Interests

The authors declare no conflict of interest.

Data Availability Statement

The data that support the findings of this study are openly available in Figshare at https://doi.org/[10.48420/c.6985935doi], reference number 1.

Keywords: alcohol oxidation · single atom catalyst · ceria · nanoparticle · adsorption · NMR relaxation.

[1] a) T. Mallat, A. Baiker, *Catal. Today* **1995**, *24*, 143–150; b) R. A. Sheldon, *Catal. Today* **1987**, *1*, 351–355; c) R. A. Sheldon, I. W. Arends, G. J. Ten Brink, A. Dijksman, *Accouts of Chemical Research* **2002**, *35*, 774–781.
[2] D. Meyer, L. Walter, G. Kolter, M. Pohl, M. Müller, K. Tittmann, *J. Am. Chem. Soc.* **2011**, *133*, 3609–3616.
[3] T. Gessner, U. Mayer, in *Ullmann's Encyclopedia of Industrial Chemistry*.
[4] C. Loch, H. Reusch, I. Ruge, R. Godelmann, T. Pflaum, T. Kuballa, S. Schumacher, D. W. Lachenmeier, *Food Chem.* **2016**, *206*, 74–77.
[5] a) D. G. Lee, U. A. Spitzer, *J. Org. Chem.* **1970**, *35*, 3589–3590; b) P. V. Prabhakaran, S. Venkatachalam, K. N. Ninan, *Eur. Polym. J.* **1999**, *35*, 1743–1746.
[6] a) T. Lu, Z. Du, J. Liu, H. Ma, J. Xu, *Green Chem.* **2013**, *15*, 2215–2221; b) L. J. Durndell, C. M. A. Parlett, N. S. Hondow, K. Wilson, A. F. Lee, *Nanoscale* **2013**, *5*, 5412–5419.
[7] a) C. M. A. Parlett, L. J. Durndell, A. Machado, G. Cibin, D. W. Bruce, N. S. Hondow, K. Wilson, A. F. Lee, *Catal. Today* **2014**, *229*, 46–55; b) C. M. A. Parlett, P. Keshwalla, S. G. Wainwright, D. W. Bruce, N. S. Hondow, K. Wilson, A. F. Lee, *ACS Catal.* **2013**, *3*, 2122–2129; c) A. Ziarko, T. J. A. Slater, M. A. Isaacs, L. J. Durndell, C. M. A. Parlett, *Catalysis Science, Technology* **2023**, *13*, 3483–3488; d) C. M. A. Parlett, D. W. Bruce, N. S. Hondow, A. F. Lee, K. Wilson, *ACS Catal.* **2011**, *1*, 636–640.
[8] a) A. S. K. Hashmi, G. J. Hutchings, *Angew. Chem. Int. Ed.* **2006**, *45*, 7896–7936; b) L. Ardemani, G. Cibin, A. J. Dent, M. A. Isaacs, G. Kyriakou, A. F. Lee, C. M. A. Parlett, S. A. Parry, K. Wilson, *Chem. Sci.* **2015**, *6*, 4940–4945.
[9] C. M. A. Parlett, M. A. Isaacs, S. K. Beaumont, L. M. Bingham, N. S. Hondow, K. Wilson, A. F. Lee, *Nat. Mater.* **2016**, *15*, 178–182.
[10] a) Y. Peng, B. Qiu, S. Ding, M. Hu, Y. Zhang, Y. Jiao, X. Fan, C. M. A. Parlett, *ChemPlusChem* **2023**, *n/a*, e202300545; b) N. Dimitratos, J. A. Lopez-Sanchez, D. Morgan, A. Carley, L. Prati, G. J. Hutchings, *Catal. Today* **2007**, *122*, 317–324.

[11] A. Abad, P. Concepción, A. Corma, H. García, *Angew. Chem. Int. Ed.* **2005**, *44*, 4066–4069.
[12] W. Fang, J. Chen, Q. Zhang, W. Deng, Y. Wang, *Chemistry* **2011**, *17*, 1247–1256.
[13] H. E. Cross, D. R. Brown, *Catal. Commun.* **2010**, *12*, 243–245.
[14] B. Qiao, A. Wang, X. Yang, L. F. Allard, Z. Jiang, Y. Cui, J. Liu, J. Li, T. Zhang, *Nat. Chem.* **2011**, *3*, 634–641.
[15] S. F. J. Hackett, R. M. Brydson, M. H. Gass, I. Harvey, A. D. Newman, K. Wilson, A. F. Lee, *Angew. Chem. Int. Ed.* **2007**, *46*, 8593–8596.
[16] T. Li, F. Liu, Y. Tang, L. Li, S. Miao, Y. Su, J. Zhang, J. Huang, H. Sun, M. Haruta, A. Wang, B. Qiao, J. Li, T. Zhang, *Angew. Chem. Int. Ed.* **2018**, *57*, 7795–7799.
[17] a) J. Jones, H. Xiong, A. T. DeLaRiva, E. J. Peterson, H. Pham, S. R. Challa, G. Qi, S. Oh, M. H. Wiebenga, X. I. Pereira Hernández, Y. Wang, A. K. Datye, *Science* **2016**, *353*, 150–154; b) Y. Guo, S. Mei, K. Yuan, D.-J. Wang, H.-C. Liu, C.-H. Yan, Y.-W. Zhang, *ACS Catal.* **2018**, *8*, 6203–6215.
[18] B. Song, D. Choi, Y. Xin, C. R. Bowers, H. Hagelin-Weaver, *Angew. Chem. Int. Ed.* **2021**, *60*, 4038–4042.
[19] S. Chen, S. Li, R. You, Z. Guo, F. Wang, G. Li, W. Yuan, B. Zhu, Y. Gao, Z. Zhang, H. Yang, Y. Wang, *ACS Catal.* **2021**, *11*, 5666–5677.
[20] B. Hu, K. Sun, Z. Zhuang, Z. Chen, S. Liu, W.-C. Cheong, C. Chen, M. Hu, X. Cao, J. Ma, R. Tu, X. Zheng, H. Xiao, X. Chen, Y. Cui, Q. Peng, C. Chen, Y. Li, *Adv. Mater.* **2022**, *34*, 2107721.
[21] a) X.-S. Huang, H. Sun, L.-C. Wang, Y.-M. Liu, K.-N. Fan, Y. Cao, *Appl. Catal. B* **2009**, *90*, 224–232; b) R. Si, M. Flytzani-Stephanopoulos, *Angew. Chem. Int. Ed.* **2008**, *47*, 2884–2887; c) N. Yi, R. Si, H. Saltsburg, M. Flytzani-Stephanopoulos, *Energy Environ. Sci.* **2010**, *3*, 831–837; d) G. Yi, H. Yang, B. Li, H. Lin, K.-i. Tanaka, Y. Yuan, *Catal. Today* **2010**, *157*, 83–88.
[22] a) X. Liu, K. Zhou, L. Wang, B. Wang, Y. Li, *J. Am. Chem. Soc.* **2009**, *131*, 3140–3141; b) L. Wang, G. Lu, D. Yang, J. Wang, Z. Zhu, Z. Wang, K. Zhou, *ChemCatChem* **2013**, *5*, 1308–1312; c) H.-X. Mai, L.-D. Sun, Y.-W. Zhang, R. Si, W. Feng, H.-P. Zhang, H.-C. Liu, C.-H. Yan, *J. Phys. Chem. B* **2005**, *109*, 24380–24385.
[23] M. A. Isaacs, C. Drivas, R. Lee, R. Palgrave, C. M. A. Parlett, D. J. Morgan, *Applied Surface Science Advances* **2023**, *18*, 100469.
[24] a) D. R. Mullins, S. H. Overbury, D. R. Huntley, *Surf. Sci.* **1998**, *409*, 307–319; b) E. Bêche, P. Charvin, D. Perarnau, S. Abanades, G. Flamant, *Surf. Interface Anal.* **2008**, *40*, 264–267.
[25] a) A. Trovarelli, *Catal. Rev.* **1996**, *38*, 439–520; b) T. Montini, M. Melchionna, M. Monai, P. Fornasiero, *Chem. Rev.* **2016**, *116*, 5987–6041; c) F. Esch, S. Fabris, L. Zhou, T. Montini, C. Africh, P. Fornasiero, G. Comelli, R. Rosei, *Science* **2005**, *309*, 752–755.
[26] L. J. Zhang, R. H. Chen, Y. Tu, X. Y. Gong, X. Cao, Q. Xu, Y. Li, B. J. Ye, Y. F. Ye, J. F. Zhu, *ACS Catal.* **2023**, *13*, 2202–2213.
[27] a) L. DeRita, J. Resasco, S. Dai, A. Boubnov, H. V. Thang, A. S. Hoffman, I. Ro, G. W. Graham, S. R. Bare, G. Pacchioni, X. Pan, P. Christopher, *Nat. Mater.* **2019**, *18*, 746–751; b) Z. Zhang, C. Feng, D. Wang, S. Zhou, R. Wang, S. Hu, H. Li, M. Zuo, Y. Kong, J. Bao, J. Zeng, *Nat. Commun.* **2022**, *13*, 2473.
[28] C. Zhang, A. Michaelides, S. J. Jenkins, *Phys. Chem. Chem. Phys.* **2011**, *13*, 22–33.
[29] a) B. C. Gates, *Trends Chem.* **2019**, *1*, 99–110; b) A. V. Crewe, J. Wall, J. Langmore, *Science* **1970**, *168*, 1338–1340.
[30] S. J. Pennycook, L. A. Boatner, *Nature* **1988**, *336*, 565–567.
[31] Q. Fu, H. Saltsburg, M. Flytzani-Stephanopoulos, *Science* **2003**, *301*, 935–938.
[32] J. Radnik, C. Mohr, P. Claus, *Phys. Chem. Chem. Phys.* **2003**, *5*, 172–177.
[33] L. Ge, T. Chen, Z. Q. Liu, F. Chen, *Catal. Today* **2014**, *224*, 209–215.
[34] a) S.-Y. Chang, A. Uehara, S. G. Booth, K. Ignatyev, J. F. W. Mosselmans, R. A. W. Dryfe, S. L. M. Schroeder, *RSC Adv.* **2015**, *5*, 6912–6918; b) X. Sun, S. R. Dawson, T. E. Parmentier, G. Malta, T. E. Davies, Q. He, L. Lu, D. J. Morgan, N. Carthey, P. Johnston, S. A. Kondrat, S. J. Freakley, C. J. Kiely, G. J. Hutchings, *Nat. Chem.* **2020**, *12*, 560–567.
[35] a) B. Qiao, J.-X. Liang, A. Wang, C.-Q. Xu, J. Li, T. Zhang, J. J. Liu, *Nano Res.* **2015**, *8*, 2913–2924; b) S. Zhao, F. Chen, S. Duan, B. Shao, T. Li, H. Tang, Q. Lin, J. Zhang, L. Li, J. Huang, N. Bion, W. Liu, H. Sun, A.-Q. Wang, M. Haruta, B. Qiao, J. Li, J. Liu, T. Zhang, *Nat. Commun.* **2019**, *10*, 3824.
[36] N. Weiher, E. A. Willneff, C. Figulla-Kroschel, M. Jansen, S. L. M. Schroeder, *Solid State Commun.* **2003**, *125*, 317–322.
[37] T. X. T. Sayle, S. C. Parker, D. C. Sayle, *Phys. Chem. Chem. Phys.* **2005**, *7*, 2936–2941.
[38] a) M. Baudin, M. Wójcik, K. Hermansson, *Surf. Sci.* **2000**, *468*, 51–61; b) U. Castanet, C. Feral-Martin, A. Demourgues, R. L. Neale, D. C. Sayle, F. Caddeo, J. M. Flitcroft, R. Caygill, B. J. Pointon, M. Molinari, J. Majimel, *ACS Appl. Mater. Interfaces* **2019**, *11*, 11384–11390.
[39] T. X. T. Sayle, S. C. Parker, C. R. A. Catlow, *Surf. Sci.* **1994**, *316*, 329–336.
[40] M. Bugnet, S. H. Overbury, Z. L. Wu, T. Epicier, *Nano Lett.* **2017**, *17*, 7652–7658.
[41] O. S. Bezkrovnyi, P. Kraszkiewicz, W. Mista, L. Kepinski, *Catal. Lett.* **2021**, *151*, 1080–1090.
[42] J. A. Hernández, S. A. Gómez, T. A. Zepeda, J. C. Fierro-González, G. A. Fuentes, *ACS Catal.* **2015**, *5*, 4003–4012.
[43] L. J. Lei, H. Liu, Z. W. Wu, Z. F. Qin, G. F. Wang, J. Y. Ma, L. Luo, W. B. Fan, J. G. Wang, *ACS Appl. Nano Mater.* **2019**, *2*, 5214–5223.
[44] a) C. D'Agostino, J. Mitchell, M. D. Mantle, L. F. Gladden, *Chem. Eur. J.* **2014**, *20*, 13009–13015; b) K. Ralphs, C. D'Agostino, R. Burch, S. Chansai, L. F. Gladden, C. Hardacre, S. L. James, J. Mitchell, S. F. R. Taylor, *Catalysis Science, Technology* **2014**, *4*, 531–539; c) C. D'Agostino, G. Brett, G. Divitini, C. Ducati, G. J. Hutchings, M. D. Mantle, L. F. Gladden, *ACS Catal.* **2017**, *7*, 4235–4241.
[45] C. D'Agostino, G. L. Brett, P. J. Miedziak, D. W. Knight, G. J. Hutchings, L. F. Gladden, M. D. Mantle, *Chem. Eur. J.* **2012**, *18*, 14426–14433.
[46] a) N. Robinson, C. D'Agostino, M. L. Johns, *Magnetic Resonance Letters* **2023**, *3*, 248–255; b) N. Robinson, E. F. May, M. L. Johns, *ACS Appl. Mater. Interfaces* **2021**, *13*, 54476–54485.
[47] D. Weber, J. Mitchell, J. McGregor, L. F. Gladden, *J. Phys. Chem. C* **2009**, *113*, 6610–6615.
[48] B. Ravel, M. Newville, *J. Synchrotron Radiat.* **2005**, *12*, 537–541.

Manuscript received: December 18, 2023
Revised manuscript received: February 16, 2024
Accepted manuscript online: April 11, 2024
Version of record online: May 24, 2024